Journal of Computational Physics 448 (2022) 110727

Contents lists available at ScienceDirect

Journal of Computational Physics

www.elsevier.com/locate/jcp

Second order approximation for a quasi-incompressible Navier-Stokes Cahn-Hilliard system of two-phase flows with variable density

Zhenlin Guo [a,1], Qing Cheng [b,*,2], Ping Lin [c,3], Chun Liu [b,2], John Lowengrub [d,4]

[a] *Mechanics Division, Beijing Computational Science Research Center, Building 9, East Zone, ZPark II, No.10 East Xibeiwang Road, Haidian District, Beijing 100193, China*
[b] *Department of Applied Mathematics, Illinois Institute of Technology, 10 West 35th Street Chicago, IL 60616, United States of America*
[c] *Division of Mathematics, University of Dundee, Dundee DD1 4HN, UK*
[d] *Department of Applied Mathematics, University of California Irvine, 540H Rowland Hall, Irvine, CA 92697, United States of America*

ARTICLE INFO

Article history:
Available online 24 September 2021

Keywords:
Phase-fields
Quasi-incompressilbe
Second order schemes
Energy stable

ABSTRACT

Phase-field model has been applied extensively and successfully for simulating two-phase flows with variable density. Several stable numerical methods have been proposed for solving such a highly nonlinear and coupled system. The key issue is to design a method such that it can preserve the (exact or slightly modified) conservative/dissipative law of energy of the fluid system at the discrete level. However, most of the existing energy stable numerical methods are restricted to only the first order accuracy in time for two-phase flow with different density. The design of a temporally second order accurate numerical method for the two-phase flows with variable density still remains challenging. In this paper, we develop several second order, robust and accurate numerical schemes for a quasi-incompressible Navier-Stokes Cahn-Hilliard model of two-phase flows with variable density which is thermodynamically consistent and was originally developed in [1] for simulating two-phase flows in complex geometries. Especially, numerical schemes proposed in this paper can preserve the mass conservation or energy dissipative law. Several numerical examples are presented to validate the robustness and accuracy of our numerical schemes.

1. Introduction

Several phase field models have been developed and computed for simulating the two phase flows with variable density and viscosity [2–11]. Some of these models are thermodynamically consistent such that the system equations satisfy the conservation laws of mass and energy dissipative/conservative law, which can be used to design the so called energy

---

[*] Corresponding author.
E-mail address: qcheng4@iit.edu (Q. Cheng).

[1] The work of Zhenlin Guo was supported in part by National Nature Science Foundation of China U1930402 and 12001035.

[2] The work of Chun Liu and Qing Cheng was supported in part by National Science Foundation DMS-1759535 and DMS-1950868 and the United States-Israel Binational Science Founation (BSF) 2024246.

[3] The work of Ping Lin was supported in part by the National Natural Science Foundation of China 11771040, 11861131004 and the Fundamental Research Funds for the Central Universities 06500073.

[4] The work of John Lowengrub is supported in part by National Science Foundation DMS-1719960, DMS-1763272 and the Simons Foundation (594598,QN) for the center for Multiscale Cell Fate Research at UC Irvine.

https://doi.org/10.1016/j.jcp.2021.110727

stable numerical methods that preserve the conservation laws at the spatially discrete level or fully discrete level (both the temporally and spatially discrete). However, most of the existing energy stable numerical methods are restricted to only the first order accuracy in time [6–8,12–16]. The main difficulty is how to temporally discretize the term $\rho\boldsymbol{u}_t$ in the momentum equation, which is consisting of a variable density ρ and velocity $\boldsymbol{u}$.

In this paper, we present three numerical methods for an existing thermodynamically consistent two phase flows with variable density and viscosity. Our numerical methods are mass conservative or energy stable which also achieve second order accuracy both temporally and spatially. The first scheme can preserve mass conservative law exactly based on Crank-Nicholson discretization. The second scheme is energy stable based on recently proposed Lagrange multiplier approach [17]. The third energy stable scheme is constructed by rewriting the quasi-incompressible Navier-Stokes Cahn-Hilliard system into an equivalent system. Numerical results are implemented to show the convergence rate and energy non-increasing for our numerical schemes. Some numerical examples are presented in capturing the interface breakup and collisions smoothly, and handling the large density and viscosity ratio. Using numerical schemes proposed, the pinch-off event and rising bubble phenomenon can be simulated efficiently which are consistent with experimental results. The reminder of this paper is structured as follows. In Section 2, we present the q-NSCH model for two phase flows with variable density and viscosity, and show that the model equations satisfy the conservation laws of mass and energy dissipative law. In Section 3, we present our numerical methods with second order accuracy, and show that numerical schemes are mass conservative, energy stable at the temporally discrete level. In Section 4, we briefly show the implementations of our numerical schemes by using a finite difference method on staggered grid. In Section 5, we show the convergence tests of our numerical methods. Several numerical examples and corresponding numerical comparisons are presented to validate our numerical schemes. Some concluding remarks are given in final Section 6.

2. Quasi-incompressible Navier-Stokes Cahn-Hilliard system

In this paper, we consider the following quasi-incompressible Navier-Stokes Cahn-Hilliard (q-NSCH) model [1] for the two-phase fluid flows with variable density and viscosity, which was originally developed for simulating two-phase flows in complex geometries. The q-NSCH model is formulated as

$$\rho\boldsymbol{u}_t+\rho\boldsymbol{u}\cdot\nabla\boldsymbol{u}+\nabla p=\nabla\cdot(\nu(c)\nabla\boldsymbol{u})+\frac{1}{3}\nabla(\nu(c)\nabla\cdot\boldsymbol{u})-\tilde{\sigma}c\nabla\mu-\rho g\boldsymbol{z}, \tag{1}$$

$$\nabla\cdot\boldsymbol{u}=\alpha\nabla\cdot(\tilde{\sigma}M(c)\nabla\mu)+\alpha^2\nabla\cdot(\tilde{\sigma}M(c)\nabla p), \tag{2}$$

$$c_t+\nabla\cdot(\boldsymbol{u}c)=\nabla\cdot(\tilde{\sigma}M(c)\nabla\mu)+\alpha\nabla\cdot(\tilde{\sigma}M(c)\nabla p), \tag{3}$$

$$\mu=f(c)-\epsilon\Delta c, \tag{4}$$

where $\boldsymbol{u}$ is the velocity of fluid, p is the pressure, c is the phase variable ($c\in[0,1]$). In particular, $c=1,0$ represents fluid 1 and fluid 2 respectively. Moreover, μ is the chemical potential and ϵ is a small parameter that relates to the thickness of the diffuse interface, g is the gravity and $\boldsymbol{z}$ is the unit vector in the vertical direction, and $\tilde{\sigma}$ is the surface tension that can be related to the physical surface tension σ through $\tilde{\sigma}=6\sqrt{2}\sigma$ [18]. We introduce the following variable density and viscosity for the two-phase flows:

$$\rho=\rho(c)=\rho_1c+\rho_2(1-c),\quad \nu=\nu(c)=\nu_1c+\nu_2(1-c), \tag{5}$$

where ρ_i and ν_i (for $i=1,2$) are constants that represent the density and viscosity of the ith fluid. The parameter $\alpha=(\rho_2-\rho_1)/\rho_2$ represents the relative density rate. The nonlinear term $F(c)=c^2(1-c)^2/4\epsilon$ is the well-known double well potential and $f(c)=F'(c)$. $M(c)=\sqrt{c^2(1-c)^2+\epsilon}$ is the degenerate mobility. Moreover, we consider the following boundary conditions:

$$\boldsymbol{u}|_{\partial\Omega}=b_{\boldsymbol{u}},\quad \nabla c\cdot\boldsymbol{n}|_{\partial\Omega}=\nabla\mu\cdot\boldsymbol{n}|_{\partial\Omega}=0, \tag{6}$$

where Ω is the computational domain, $\partial\Omega$ denotes the domain boundary, and $\boldsymbol{n}$ is unit outward normal vector of boundary.

Remark 2.1. Here we briefly show how we define the variable density and the mass-averaged velocity.

We take an arbitrary material volume V in Ω, where the two fluids are labeled by $i=1,2$ and fill the volumes V_i separately ($V=V_1\cup V_2$). We then introduce the volume fraction c_i for the ith fluid such that $c_i=V_i/V$. Further, we assume that the two fluids can mix along the interfacial region and the volume of the single fluid does not change after mixing. Then, within the material volume V, c_i satisfy the condition $c_1+c_2=1$. Let $M=M_1+M_2$ be the total mass of the mixture, and M_i be the mass of the ith fluid in the volume. We now introduce the local volume-averaged mass density taken over the sufficient small volume V for each fluid $\tilde{\rho}_i=M_i/V$, and the actual local mass density for each fluid $\rho_i=M_i/V_i$. It should be noted that for incompressible components, ρ_i are assumed to be uniform constants. Having in mind the definition of volume fraction c_i, we obtain the relation between the volume-averaged mass densities and the local mass densities,

$$c_i = \frac{\tilde{\rho}_i}{\rho_i} \text{ and } \frac{\tilde{\rho}_1}{\rho_1} + \frac{\tilde{\rho}_2}{\rho_2} = 1. \tag{7}$$

We then define the volume-averaged mass density for the mixture as

$$\rho = \frac{M}{V} = \frac{M_1 + M_2}{V} = \tilde{\rho}_1 + \tilde{\rho}_2 = c_1\rho_1 + c_2\rho_2. \tag{8}$$

By using c_1 as the phase variable $c = c_1$ and $c_2 = 1 - c$, the variable density then reads

$$\rho = c\rho_1 + (1-c)\rho_2. \tag{9}$$

Now we suppose that the two fluids move with different velocities $\boldsymbol{u}_i(\boldsymbol{x}, t)$ for $i = 1, 2$. The equation of mass balance for each fluid within the material volume V can then be written in the form (Lowengrub & Truskinovsky 1998; Boyer 2002; Abels et al. 2012):

$$\frac{\partial \tilde{\rho}_i}{\partial t} + \nabla \cdot (\tilde{\rho}_i \boldsymbol{u}_i) = 0. \tag{10}$$

We then introduce the mass-averaged velocity for the mixture as

$$\rho \boldsymbol{u} = \tilde{\rho}_1 \boldsymbol{u}_1 + \tilde{\rho}_2 \boldsymbol{u}_2. \tag{11}$$

Substituting the density (8) and mass-averaged velocity (11) into (10), we obtain the mass balance for the mixture of two fluids,

$$\rho_t + \nabla \cdot (\rho \boldsymbol{u}) = 0. \tag{12}$$

We then show how we obtain the quasi-incompressibility from the mass conservation. Substituting Eq. (9) into Eq. (12), we obtain

$$\begin{aligned} &\rho_t + \rho \nabla \cdot \boldsymbol{u} + \boldsymbol{u} \cdot \nabla \rho \\ =&(\rho_1 - \rho_2)c_t + \Big(\rho_1 c + \rho_2(1-\phi)\Big)\nabla \cdot \boldsymbol{u} + (\rho_1 - \rho_2)\boldsymbol{u} \cdot \nabla c \\ =&(\rho_1 - \rho_2)\Big(c_t + \nabla \cdot (c\boldsymbol{u})\Big) + \rho_2 \nabla \cdot \boldsymbol{u} = 0, \end{aligned} \tag{13}$$

which can be rewritten as

$$\begin{aligned} (\rho_1 - \rho_2)\Big(c_t + \nabla \cdot (c\boldsymbol{u})\Big) &= -\rho_2 \nabla \cdot \boldsymbol{u}, \\ c_t + \nabla \cdot (c\boldsymbol{u}) &= \frac{\rho_2 - \rho_2}{\rho_2} \nabla \cdot \boldsymbol{u}, \end{aligned} \tag{14}$$

such that

$$\alpha \nabla \cdot \boldsymbol{u} = c_t + \nabla \cdot (c\boldsymbol{u}). \tag{15}$$

Where the velocity field is not divergence free along the interfacial region, and is termed as the quasi-incompressibility.

Before we demonstrate our numerical schemes, we show the following conservation laws of mass and energy dissipative law for q-NSCH system (1)-(4).

Theorem 2.1. *The quasi-incompressible Navier-Stokes Cahn-Hilliard (q-NSCH) system equations* (1)-(4) *satisfies the following mass conservation law,*

$$\rho_t + \nabla \cdot (\rho \boldsymbol{u}) = 0. \tag{16}$$

Proof. Multiplying α on both sides for Eq. (3), we obtain

$$\alpha c_t + \alpha \nabla \cdot (\boldsymbol{u} c) = \alpha \nabla \cdot (\tilde{\sigma} M(c) \nabla \mu) + \alpha^2 \nabla \cdot (\tilde{\sigma} M(c) \nabla p). \tag{17}$$

Substituting the right-hand side of Eq. (17) by Eq. (2), we obtain

$$\alpha c_t + \alpha \nabla \cdot (\boldsymbol{u} c) = \nabla \cdot \boldsymbol{u}. \tag{18}$$

Noticing the definition $\alpha = (\rho_2 - \rho_1)/\rho_2$, we derive from Eq. (18)

$$(\rho_2 - \rho_1) c_t + (\rho_2 - \rho_1) \nabla \cdot (\boldsymbol{u} c) = \rho_2 \nabla \cdot \boldsymbol{u}. \tag{19}$$

We then rewrite Eq. (19) as

$$(\rho_2 - \rho_1) c_t + (\rho_2 - \rho_1)(c \nabla \cdot \boldsymbol{u} + \boldsymbol{u} \cdot \nabla c) = \rho_2 \nabla \cdot \boldsymbol{u}. \tag{20}$$

By using the definition of variable density $\rho = \rho(c) = \rho_1 c + \rho_2 (1 - c)$, we obtain

$$\rho_t = (\rho_1 - \rho_2) c_t, \quad \nabla \rho = (\rho_1 - \rho_2) \nabla c. \tag{21}$$

Combing Eqs. (20) and (21), we obtain the desired mass conservation law (16). □

Theorem 2.2. *The q-NSCH system equations (1)-(4) satisfy the following energy dissipative law:*

$$\begin{aligned} \frac{d}{dt} \int_\Omega \left(\frac{1}{2} \rho \boldsymbol{u}^2 + \frac{\tilde{\sigma}\epsilon}{2} |\nabla c|^2 + \tilde{\sigma} F(c) \right) d\boldsymbol{x} = &- \nu(c) \|\nabla \boldsymbol{u}\|^2 - \frac{1}{3} \nu(c) \|\nabla \cdot \boldsymbol{u}\|^2 \\ &- \tilde{\sigma} M(c) \|\nabla \mu + \alpha \nabla p\|^2. \end{aligned} \tag{22}$$

Proof. Taking inner product of Eqs. (1) and (16) with $\boldsymbol{u}$, adding them together and applying the integration by parts together with homogeneous Dirichlet boundary condition, we derive,

$$\begin{aligned} &\int_\Omega \left(\frac{1}{2} \rho (\boldsymbol{u}^2)_t + \frac{1}{2} \rho \boldsymbol{u} \cdot \nabla (\boldsymbol{u}^2) + \frac{1}{2} \rho_t \boldsymbol{u}^2 + \frac{1}{2} \nabla \cdot (\rho \boldsymbol{u}) \boldsymbol{u}^2 \right) d\boldsymbol{x} \\ &= -(\boldsymbol{u}, \nabla p) - \nu(c) \|\nabla \boldsymbol{u}\|^2 - \frac{1}{3} \nu(c) \|\nabla \cdot \boldsymbol{u}\|^2 - (c\boldsymbol{u}, \nabla \mu) - \int_\Omega \rho g \boldsymbol{z} \cdot \boldsymbol{u} \, d\boldsymbol{x}. \end{aligned} \tag{23}$$

With the help of the following identity and integration by parts

$$\int_\Omega \left(\frac{1}{2} \rho \boldsymbol{u} \cdot \nabla (\boldsymbol{u}^2) + \frac{1}{2} \nabla \cdot (\rho \boldsymbol{u}) \boldsymbol{u}^2 \right) d\boldsymbol{x} = 0, \tag{24}$$

Eq. (23) can be simplified to

$$\frac{d}{dt} \int_\Omega \frac{1}{2} \rho \boldsymbol{u}^2 \, d\boldsymbol{x} = - (\boldsymbol{u}, \nabla p) - \nu(c) \|\nabla \boldsymbol{u}\|^2 - \frac{1}{3} \nu(c) \|\nabla \cdot \boldsymbol{u}\|^2 - (c\boldsymbol{u}, \nabla \mu) - \int_\Omega \rho g \boldsymbol{z} \cdot \boldsymbol{u} \, d\boldsymbol{x}. \tag{25}$$

By using the mass conservation (16), we obtain

$$\int_\Omega \rho g \boldsymbol{z} \cdot \boldsymbol{u} \, d\boldsymbol{x} = \int_\Omega \rho g \boldsymbol{u} \cdot \nabla z \cdot \, d\boldsymbol{x} = - \int_\Omega \nabla \cdot (\rho \boldsymbol{u}) g z \, d\boldsymbol{x} = \int_\Omega \rho_t g z \, d\boldsymbol{x}. \tag{26}$$

Such that we can rewrite Eq. (25) as

$$\frac{d}{dt} \int_\Omega \left(\frac{1}{2} \rho \boldsymbol{u}^2 + \rho g z \right) d\boldsymbol{x} = - (\boldsymbol{u}, \nabla p) - \nu(c) \|\nabla \boldsymbol{u}\|^2 - \frac{1}{3} \nu(c) \|\nabla \cdot \boldsymbol{u}\|^2 - (c\boldsymbol{u}, \nabla \mu). \tag{27}$$

Taking inner product of Eq. (2) with p and applying the integration by parts, we obtain

$$(\nabla \cdot \boldsymbol{u}, p) = -(\boldsymbol{u}, \nabla p) = -(\alpha \tilde{\sigma} M(c) \nabla \mu, \nabla p) - (\alpha^2 \tilde{\sigma} M(c) \nabla p, \nabla p). \tag{28}$$

Taking inner product of Eq. (3) with μ and applying the integration by parts, we obtain

$$(c_t, \mu) + (\nabla \cdot (\boldsymbol{u} c), \mu) = -(\tilde{\sigma} M(c) \nabla \mu, \nabla \mu) - (\alpha \tilde{\sigma} M(c) \nabla p, \nabla \mu). \tag{29}$$

Taking inner product of Eq. (4) with c_t and applying the integration by parts, we obtain

$$\frac{d}{dt} \int_\Omega \left(\frac{\tilde{\sigma}\epsilon}{2} |\nabla c|^2 + \tilde{\sigma} F(c) \right) d\boldsymbol{x} = (c_t, \mu). \tag{30}$$

Combing Eqs. (27)-(30), we obtain the following energy dissipative law:

$$\frac{d}{dt}\int_{\Omega}\left(\frac{1}{2}\rho\boldsymbol{u}^2+\rho gz+\frac{\tilde{\sigma}\epsilon}{2}|\nabla c|^2+\tilde{\sigma}F(c)\right)d\boldsymbol{x}=-\nu(c)\|\nabla\boldsymbol{u}\|^2-\frac{1}{3}\nu(c)\|\nabla\cdot\boldsymbol{u}\|^2 \\ -\tilde{\sigma}M(c)\|\nabla\mu+\alpha\nabla p\|^2. \quad \square \tag{31}$$

3. Numerical methods

In this section, we construct three robust, second order numerical schemes for q-NSCH system equations (1)-(4). The goals of these schemes are preserving the conservation laws of mass and energy dissipative law at the temporal discrete level.

3.1. Scheme 1: mass conservative scheme

$$\rho^{n+\frac{1}{2}}\boldsymbol{u}_{\bar{t}}+\rho^{n+\frac{1}{2}}\boldsymbol{u}^{n+\frac{1}{2}}\cdot\nabla\boldsymbol{u}^{n+\frac{1}{2}}+\nabla p^{n+\frac{1}{2}}=\nabla\cdot(\nu(c^{n+\frac{1}{2}})\nabla\boldsymbol{u}^{n+\frac{1}{2}}) \\ +\frac{1}{3}\nabla(\nu(c^{n+\frac{1}{2}})\nabla\cdot\boldsymbol{u}^{n+\frac{1}{2}})-\tilde{\sigma}c^{n+\frac{1}{2}}\nabla\mu^{n+\frac{1}{2}}-\rho^{n+\frac{1}{2}}g\boldsymbol{z}, \tag{32}$$

$$\nabla\cdot\boldsymbol{u}^{n+\frac{1}{2}}=\alpha\nabla\cdot(\tilde{\sigma}M(c^{n+\frac{1}{2}})\nabla\mu^{n+\frac{1}{2}})+\alpha^2\nabla\cdot(\tilde{\sigma}M(c^{n+\frac{1}{2}})\nabla p^{n+\frac{1}{2}}), \tag{33}$$

$$c_{\bar{t}}+\nabla\cdot(\boldsymbol{u}^{n+\frac{1}{2}}c^{n+\frac{1}{2}})=\nabla\cdot(\tilde{\sigma}M(c^{n+\frac{1}{2}})\nabla\mu^{n+\frac{1}{2}}) \\ +\alpha\nabla\cdot(\tilde{\sigma}M(c^{n+\frac{1}{2}})\nabla p^{n+\frac{1}{2}}), \tag{34}$$

$$\mu^{n+\frac{1}{2}}=f(c^{n+1},c^n)-\epsilon\Delta c^{n+\frac{1}{2}}, \tag{35}$$

with the following boundary conditions

$$\boldsymbol{u}^{n+1}=b_{\boldsymbol{u}},\ \ \boldsymbol{n}\cdot\nabla c^{n+1}=\boldsymbol{n}\cdot\nabla\mu^{n+1}=0 \quad \text{on} \quad \partial\Omega. \tag{36}$$

Here

$$f(c^{n+1},c^n)=\frac{1}{4}\left(c^{n+1}+c^n-1\right)\left((c^{n+1})^2+(c^n)^2-c^{n+1}-c^n\right) \\ =\frac{1}{4}c^{n+1}\left((c^{n+1})^2+(c^n)^2-c^{n+1}-c^n\right), \tag{37}$$

$$*^{n+\frac{1}{2}}=\frac{1}{2}(*^{n+1}+*^n) \quad (*:\ p,\ c,\ \mu), \tag{38}$$

$$*_{\bar{t}}=\frac{*^{n+1}-*^n}{\delta t}, \tag{39}$$

$f(c^{n+1},c^n)$ is a second order approximation of $f(c)=\frac{1}{2}(c^2-c)(2c-1)$. We would like to mention that there are also some second order approximations for nonlinear term $f(c)$ developed for Cahn-Hilliard type equations in [17,19]. The boundary condition (6) is considered. Below we prove that the second order approximation of mass conservation law is achieved in time discrete level for scheme 1.

Theorem 3.1. *The nonlinear scheme (32)-(35) satisfies the following discrete mass conservation law:*

$$\rho_{\bar{t}}+\nabla\cdot(\rho^{n+\frac{1}{2}}\boldsymbol{u}^{n+\frac{1}{2}})=0. \tag{40}$$

Proof. Multiplying Eq. (33) by $1/\alpha$ on both sides, we obtain

$$\frac{1}{\alpha}\nabla\cdot\boldsymbol{u}^{n+\frac{1}{2}}=\nabla\cdot(\tilde{\sigma}M(c^{n+\frac{1}{2}})\nabla\mu^{n+\frac{1}{2}})+\alpha\nabla\cdot(\tilde{\sigma}M(c^{n+\frac{1}{2}})\nabla p^{n+\frac{1}{2}}). \tag{41}$$

Substituting the right-hand side of Eq. (34) by Eq. (41), we obtain

$$c_{\bar{t}}+\nabla\cdot(\boldsymbol{u}^{n+\frac{1}{2}}c^{n+\frac{1}{2}})=\frac{1}{\alpha}\nabla\cdot\boldsymbol{u}^{n+\frac{1}{2}}. \tag{42}$$

Multiplying $\rho_1-\rho_2$ on both sides of Eq. (42), we obtain

$$(\rho_1-\rho_2)c_{\bar{t}}+(\rho_1-\rho_2)(c^{n+\frac{1}{2}}\nabla\cdot\boldsymbol{u}^{n+\frac{1}{2}}+\boldsymbol{u}^{n+\frac{1}{2}}\cdot\nabla c^{n+\frac{1}{2}})=\rho_2\nabla\cdot\boldsymbol{u}^{n+\frac{1}{2}}. \tag{43}$$

Such that

$$(\rho_1-\rho_2)c_{\bar{t}}+\big((\rho_1-\rho_2)c^{n+\frac{1}{2}}-\rho_2\big)\nabla\cdot\boldsymbol{u}^{n+\frac{1}{2}}+(\rho_1-\rho_2)\boldsymbol{u}^{n+\frac{1}{2}}\cdot\nabla c^{n+\frac{1}{2}}=0. \tag{44}$$

With the help of the variable density $\rho=\rho(c)=\rho_1 c+\rho_2(1-c)$, and the following identities,

$$\rho_{\bar{t}}=(\rho_1-\rho_2)c_{\bar{t}}, \tag{45}$$

$$\nabla\rho^{n+\frac{1}{2}}=(\rho_1-\rho_2)\nabla c^{n+\frac{1}{2}}, \tag{46}$$

$$\rho^{n+\frac{1}{2}}=\rho_1 c^{n+\frac{1}{2}}+\rho_2(1-c^{n+\frac{1}{2}}). \tag{47}$$

We derive the discrete mass conservation law (40) from Eq. (44). □

3.2. Scheme 2: a Lagrange multiplier approach

In this subsection we introduce a Lagrange multiplier approach [17] to construct another second order, mass conservative and energy stable scheme for q-NSCH model:

$$\begin{aligned}&\rho^{n+\frac{1}{2}}\boldsymbol{u}_{\bar{t}}+\xi^{n+\frac{1}{2}}\rho^{n+\frac{1}{2}}\boldsymbol{u}^{n+\frac{1}{2}}\cdot\nabla\boldsymbol{u}^{n+\frac{1}{2}}+\nabla p^{n+\frac{1}{2}}=\nabla\cdot(\nu(c^{n+\frac{1}{2}})\nabla\boldsymbol{u}^{n+\frac{1}{2}})\\&+\frac{1}{3}\nabla(\nu(c^{n+\frac{1}{2}})\nabla\cdot\boldsymbol{u}^{n+\frac{1}{2}})-\tilde{\sigma}c^{n+\frac{1}{2}}\nabla\mu^{n+\frac{1}{2}}-\rho^{n+\frac{1}{2}}g\boldsymbol{z},\end{aligned} \tag{48}$$

$$(\xi^{n+\frac{1}{2}}\rho^{n+\frac{1}{2}}\boldsymbol{u}^{n+\frac{1}{2}}\cdot\nabla\boldsymbol{u}^{n+\frac{1}{2}},\boldsymbol{u}^{n+\frac{1}{2}})=(\rho_{\bar{t}},\frac{(\boldsymbol{u}^{n+1})^2+(\boldsymbol{u}^n)^2}{2}), \tag{49}$$

$$\nabla\cdot\boldsymbol{u}^{n+\frac{1}{2}}=\alpha\nabla\cdot(\tilde{\sigma}M(c^{n+\frac{1}{2}})\nabla\mu^{n+\frac{1}{2}})+\alpha^2\nabla\cdot(\tilde{\sigma}M(c^{n+\frac{1}{2}})\nabla p^{n+\frac{1}{2}}), \tag{50}$$

$$c_{\bar{t}}+\nabla\cdot(\boldsymbol{u}^{n+\frac{1}{2}}c^{n+\frac{1}{2}})=\nabla\cdot(\tilde{\sigma}M(c^{n+\frac{1}{2}})\nabla\mu^{n+\frac{1}{2}})+\alpha\nabla\cdot(\tilde{\sigma}M(c^{n+\frac{1}{2}})\nabla p^{n+\frac{1}{2}}), \tag{51}$$

$$\mu^{n+\frac{1}{2}}=f(c^{n+1},c^n)-\epsilon\Delta c^{n+\frac{1}{2}}, \tag{52}$$

with the boundary conditions (36). Here ξ is a Lagrange multiplier that enforces the energy stability, $f(c^{n+1},c^n)$ is given in (37).

Theorem 3.2. *Scheme 2 (48)-(52) satisfies the discrete mass conservation law (40).*

Proof. Following Theorem 3.1, we can show that Scheme 2 also satisfies the property of mass conservation. □

Remark 3.1. Equation (49) is a second order approximation of the following equality

$$(\frac{1}{2}\rho_t,\boldsymbol{u}^2)=(\frac{1}{2}\rho\boldsymbol{u},\nabla\boldsymbol{u}^2)=(\rho\boldsymbol{u}\cdot\nabla\boldsymbol{u},\boldsymbol{u}), \tag{53}$$

where we use mass conservative law $\rho_t+\nabla\cdot(\rho\boldsymbol{u})=0$. Observed from (53), in continue case, Lagrange multiplier ξ is equal to 1.

Theorem 3.3. *Scheme 2 (48)-(52) satisfies the following discrete energy dissipative law:*

$$\begin{aligned}E_{\bar{t}}\le&-\tilde{\sigma}M(c^{n+\frac{1}{2}})\|\nabla\mu^{n+\frac{1}{2}}+\alpha\nabla p^{n+\frac{1}{2}}\|^2\\&-\nu(c^{n+\frac{1}{2}})\|\nabla\boldsymbol{u}^{n+1}\|^2-\frac{1}{3}\nu(c^{n+\frac{1}{2}})\|\nabla\cdot\boldsymbol{u}^{n+1}\|^2,\end{aligned} \tag{54}$$

where

$$E^n=\int_\Omega\left(\frac{1}{2}\rho^n|u^n|^2+\frac{\tilde{\sigma}\epsilon}{2}|\nabla c^n|^2+\tilde{\sigma}F(c^n)\right)d\boldsymbol{x} \tag{55}$$

is the total energy of the discrete system.

Proof. Taking the inner produce of Eqs. (48) and (40) with $\boldsymbol{u}^{n+\frac{1}{2}}$, and adding them together we obtain

$$\begin{aligned}&\frac{1}{2}\rho^{n+\frac{1}{2}}|\boldsymbol{u}|^2_{\bar{t}}+(\xi^{n+\frac{1}{2}}\rho^{n+\frac{1}{2}}\boldsymbol{u}^{n+\frac{1}{2}}\cdot\nabla\boldsymbol{u}^{n+\frac{1}{2}},\boldsymbol{u}^{n+\frac{1}{2}})=-\boldsymbol{u}^{n+\frac{1}{2}}\cdot\nabla p^{n+\frac{1}{2}}\\&-\nu(c^{n+\frac{1}{2}})|\nabla\boldsymbol{u}^{n+\frac{1}{2}}|^2-\frac{1}{3}\nu(c^{n+\frac{1}{2}})|\nabla\cdot\boldsymbol{u}^{n+\frac{1}{2}}|^2-\tilde{\sigma}c^{n+\frac{1}{2}}\nabla\mu^{n+\frac{1}{2}}\cdot\boldsymbol{u}^{n+\frac{1}{2}}-\rho^{n+\frac{1}{2}}g\boldsymbol{z}\cdot\boldsymbol{u}^{n+\frac{1}{2}}.\end{aligned} \tag{56}$$

Applying the following identity and the discrete mass conservation (40),

$$\begin{aligned}\int_\Omega \rho^{n+\frac12} g\boldsymbol{z}\cdot\boldsymbol{u}^{n+\frac12}\,d\boldsymbol{x} = \int_\Omega \rho^{n+\frac12} g\boldsymbol{u}^{n+\frac12}\cdot\nabla z\,d\boldsymbol{x} = -\int_\Omega gz\nabla\cdot\left(\rho^{n+\frac12}\boldsymbol{u}^{n+\frac12}\right)\,d\boldsymbol{x}\\ = \int_\Omega \rho_{\bar t} gz\,d\boldsymbol{x},\end{aligned}\tag{57}$$

and using equation (49), we obtain

$$\begin{aligned}&\frac12\rho^{n+\frac12}|\boldsymbol{u}|^2_{\bar t} + \frac12\rho_{\bar t}\frac{|\boldsymbol{u}^{n+1}|^2+|\boldsymbol{u}^n|^2}{2} + \rho_{\bar t} gz\\ &= -\boldsymbol{u}^{n+\frac12}\cdot\nabla p^{n+\frac12} - \nu(c^{n+\frac12})|\nabla\boldsymbol{u}^{n+\frac12}|^2\\ &-\frac13\nu(c^{n+\frac12})|\nabla\cdot\boldsymbol{u}^{n+\frac12}|^2 - \tilde\sigma c^{n+\frac12}\nabla\mu^{n+\frac12}\cdot\boldsymbol{u}^{n+\frac12}.\end{aligned}\tag{58}$$

With the help of the following identity:

$$\frac12\rho^{n+\frac12}|\boldsymbol{u}|^2_{\bar t} + \frac12\rho_{\bar t}\frac{|\boldsymbol{u}^{n+1}|^2+|\boldsymbol{u}^n|^2}{2} = \frac{1}{2\Delta t}\rho^{n+1}|\boldsymbol{u}^{n+1}|^2 - \frac{1}{2\Delta t}\rho^n|\boldsymbol{u}^n|^2,\tag{59}$$

we can rewrite Eq. (58) as

$$\begin{aligned}\frac12(\rho|\boldsymbol{u}|^2)_{\bar t} + \rho_{\bar t} gz = &-\boldsymbol{u}^{n+\frac12}\cdot\nabla p^{n+\frac12} - \nu(c^{n+\frac12})|\nabla\boldsymbol{u}^{n+\frac12}|^2\\ &-\frac13\nu(c^{n+\frac12})|\nabla\cdot\boldsymbol{u}^{n+\frac12}|^2 - \tilde\sigma c^{n+\frac12}\nabla\mu^{n+\frac12}\cdot\boldsymbol{u}^{n+\frac12}.\end{aligned}\tag{60}$$

Taking the inner product of Eq. (50) with $p^{n+\frac12}$, we obtain

$$\begin{aligned}\left(\nabla\cdot\boldsymbol{u}^{n+\frac12}\right)p^{n+\frac12} = &-\alpha\tilde\sigma M(c^{n+\frac12})\left(\nabla\mu^{n+\frac12}\cdot\nabla p^{n+\frac12}\right)\\ &-\alpha^2\tilde\sigma M(c^{n+\frac12})|\nabla p^{n+\frac12}|^2.\end{aligned}\tag{61}$$

Taking the inner product of Eq. (51) with $\mu^{n+\frac12}$, we obtain

$$\begin{aligned}c_{\bar t}\mu^{n+\frac12} - c^{n+\frac12}\nabla\mu^{n+\frac12}\cdot\boldsymbol{u}^{n+\frac12} = &-\tilde\sigma M(c^{n+\frac12})|\nabla\mu^{n+\frac12}|^2\\ &-\alpha\tilde\sigma M(c^{n+\frac12})\nabla p^{n+\frac12}\cdot\nabla\mu^{n+\frac12}.\end{aligned}\tag{62}$$

Taking the inner product of Eq. (52) with $c_{\bar t}$, we obtain

$$\mu^{n+\frac12}c_{\bar t} = \tilde\sigma F_{\bar t}(c) + \frac{\tilde\sigma\epsilon}{2}|\nabla c|^2_{\bar t}.\tag{63}$$

Combine Eqs. (60)-(63), we obtain the energy stability of our numerical method:

$$\begin{aligned}E_{\bar t} = &-\nu(c)^{n+\frac12}|\nabla\boldsymbol{u}^{n+\frac12}|^2 - \frac13\nu(c)^{n+\frac12}|\nabla\cdot\boldsymbol{u}^{n+\frac12}|^2\\ &-M(c)^{n+\frac12}|\nabla\mu^{n+\frac12}+\alpha\nabla p^{n+\frac12}|^2 \le 0.\quad\square\end{aligned}\tag{64}$$

3.3. *Scheme 3: reformulated form*

In this subsection, we construct the third robust, second order numerical scheme for q-NSCH model, which preserves the conservation laws of mass and energy at the temporal discrete level. Before we show the scheme, we first reformulate the model equations (1)-(4): multiplying the mass conservation (16) by $\boldsymbol{u}/2$ and adding it to the momentum equation (1), we obtain

$$\begin{aligned}\rho\boldsymbol{u}_t + \rho\boldsymbol{u}\cdot\nabla\boldsymbol{u} + \frac12(\rho_t + \nabla\cdot(\rho\boldsymbol{u}))\boldsymbol{u} + \nabla p =&\nabla\cdot(\nu(c)\nabla\boldsymbol{u}) + \frac13\nabla(\nu(c)\nabla\cdot\boldsymbol{u})\\ &-\tilde\sigma c\nabla\mu - \rho g\boldsymbol{z}.\end{aligned}\tag{65}$$

We then rewrite the above as

$$\sqrt{\rho}(\sqrt{\rho}\boldsymbol{u})_t + \rho\boldsymbol{u}\cdot\nabla\boldsymbol{u} + \frac{1}{2}\nabla\cdot(\rho\boldsymbol{u})\boldsymbol{u} + \nabla p = \nabla\cdot(\nu(c)\nabla\boldsymbol{u}) + \frac{1}{3}\nabla(\nu(c)\nabla\cdot\boldsymbol{u}) - \tilde{\sigma}c\nabla\mu - \rho g\boldsymbol{z}. \tag{66}$$

The reformulated system equations then read as:

$$\sqrt{\rho}(\sqrt{\rho}\boldsymbol{u})_t + \rho\boldsymbol{u}\cdot\nabla\boldsymbol{u} + \frac{1}{2}\nabla\cdot(\rho\boldsymbol{u})\boldsymbol{u} + \nabla p = \nabla\cdot(\nu(c)\nabla\boldsymbol{u}) + \frac{1}{3}\nabla(\nu(c)\nabla\cdot\boldsymbol{u}) - \tilde{\sigma}c\nabla\mu - \rho g\boldsymbol{z}, \tag{67}$$

$$\nabla\cdot\boldsymbol{u} = \alpha\nabla\cdot(\tilde{\sigma}M(c)\nabla\mu) + \alpha^2\nabla\cdot(\tilde{\sigma}M(c)\nabla p), \tag{68}$$

$$c_t + \nabla\cdot(\boldsymbol{u}c) = \nabla\cdot(\tilde{\sigma}M(c)\nabla\mu) + \alpha\nabla\cdot(\tilde{\sigma}M(c)\nabla p), \tag{69}$$

$$\mu = f(c) - \epsilon\Delta c. \tag{70}$$

We now show Scheme 3 for the reformulated system Eqs. (67)-(70):

$$\sqrt{\rho}^{n+\frac{1}{2}}(\sqrt{\rho}\boldsymbol{u})_{\bar{t}} + \rho^{n+\frac{1}{2}}\boldsymbol{u}^{n+\frac{1}{2}}\cdot\nabla\bar{\boldsymbol{u}}^{n+\frac{1}{2}} + \nabla p^{n+\frac{1}{2}} + \frac{1}{2}\nabla\cdot(\rho^{n+\frac{1}{2}}\boldsymbol{u}^{n+\frac{1}{2}})\bar{\boldsymbol{u}}^{n+\frac{1}{2}}$$
$$= \nabla\cdot(\nu(c^{n+\frac{1}{2}})\nabla\bar{\boldsymbol{u}}^{n+\frac{1}{2}}) + \frac{1}{3}\nabla(\nu(c^{n+\frac{1}{2}})\nabla\cdot\bar{\boldsymbol{u}}^{n+\frac{1}{2}}) - \tilde{\sigma}c^{n+\frac{1}{2}}\nabla\mu^{n+\frac{1}{2}} - \rho^{n+\frac{1}{2}}g\boldsymbol{z}, \tag{71}$$

$$\nabla\cdot\bar{\boldsymbol{u}}^{n+\frac{1}{2}} = \alpha\nabla\cdot(\tilde{\sigma}M(c^{n+\frac{1}{2}})\nabla\mu^{n+\frac{1}{2}}) + \alpha^2\nabla\cdot(\tilde{\sigma}M(c^{n+\frac{1}{2}})\nabla p^{n+\frac{1}{2}}), \tag{72}$$

$$c_{\bar{t}} + \nabla\cdot(\bar{\boldsymbol{u}}^{n+\frac{1}{2}}c^{n+\frac{1}{2}}) = \nabla\cdot(\tilde{\sigma}M(c^{n+\frac{1}{2}})\nabla\mu^{n+\frac{1}{2}}) + \alpha\nabla\cdot(\tilde{\sigma}M(c^{n+\frac{1}{2}})\nabla p^{n+\frac{1}{2}}), \tag{73}$$

$$\mu^{n+\frac{1}{2}} = f(c^{n+1}, c^n) - \epsilon\Delta c^{n+\frac{1}{2}}, \tag{74}$$

with the boundary conditions (36). Here we define

$$\sqrt{\rho}^{n+\frac{1}{2}} = \frac{\sqrt{\rho^{n+1}} + \sqrt{\rho^n}}{2}, \tag{75}$$

$$(\sqrt{\rho}\boldsymbol{u})_{\bar{t}} = \frac{\sqrt{\rho^{n+1}}\boldsymbol{u}^{n+1} - \sqrt{\rho^n}\boldsymbol{u}^n}{\delta t}, \tag{76}$$

$$\bar{\boldsymbol{u}}^{n+\frac{1}{2}} = \frac{\sqrt{\rho^{n+1}}\boldsymbol{u}^{n+1} + \sqrt{\rho^n}\boldsymbol{u}^n}{\sqrt{\rho^{n+1}} + \sqrt{\rho^n}}. \tag{77}$$

Moreover, $f(c^{n+1}, c^n)$ is given in (37). We would like to mention that there are also some second order approximations for nonlinear term $f(c)$ are developed for Cahn-Hilliard type equations in [17,19]. The boundary condition (6) is considered. Below we prove that the second order approximation of mass conservation law is achieved in time discrete level.

Theorem 3.4. *The nonlinear scheme* (71)-(74) *satisfies the following discrete mass conservation law:*

$$\rho_{\bar{t}} + \nabla\cdot(\rho^{n+\frac{1}{2}}\bar{\boldsymbol{u}}^{n+\frac{1}{2}}) = 0. \tag{78}$$

Proof. Multiplying Eq. (72) by $1/\alpha$ on both side, we obtain

$$\frac{1}{\alpha}\nabla\cdot\bar{\boldsymbol{u}}^{n+\frac{1}{2}} = \nabla\cdot(\tilde{\sigma}M(c^{n+\frac{1}{2}})\nabla\mu^{n+\frac{1}{2}}) + \alpha\nabla\cdot(\tilde{\sigma}M(c^{n+\frac{1}{2}})\nabla p^{n+\frac{1}{2}}). \tag{79}$$

Substituting the right-hand side of Eq. (73) by Eq. (79), we obtain

$$c_{\bar{t}} + \nabla\cdot(\bar{\boldsymbol{u}}^{n+\frac{1}{2}}c^{n+\frac{1}{2}}) = \frac{1}{\alpha}\nabla\cdot\bar{\boldsymbol{u}}^{n+\frac{1}{2}}. \tag{80}$$

Multiplying $\rho_1 - \rho_2$ on both sides of Eq. (80), we obtain

$$(\rho_1 - \rho_2)c_{\bar{t}} + (\rho_1 - \rho_2)(c^{n+\frac{1}{2}}\nabla\cdot\bar{\boldsymbol{u}}^{n+\frac{1}{2}} + \bar{\boldsymbol{u}}^{n+\frac{1}{2}}\cdot\nabla c^{n+\frac{1}{2}}) = \rho_2\nabla\cdot\bar{\boldsymbol{u}}^{n+\frac{1}{2}}. \tag{81}$$

Such that

$$(\rho_1 - \rho_2)c_{\bar{t}} + \big((\rho_1 - \rho_2)c^{n+\frac{1}{2}} - \rho_2\big)\nabla\cdot\bar{\boldsymbol{u}}^{n+\frac{1}{2}} + (\rho_1 - \rho_2)\bar{\boldsymbol{u}}^{n+\frac{1}{2}}\cdot\nabla c^{n+\frac{1}{2}} = 0. \tag{82}$$

With the help of the variable density $\rho = \rho(c) = \rho_1 c + \rho_2(1 - c)$, and the following identities,

$$\rho_{\bar{t}} = (\rho_1 - \rho_2)c_{\bar{t}}, \tag{83}$$

$$\nabla \rho^{n+\frac{1}{2}} = (\rho_1 - \rho_2)\nabla c^{n+\frac{1}{2}}, \tag{84}$$

$$\rho^{n+\frac{1}{2}} = \rho_1 c^{n+\frac{1}{2}} + \rho_2(1 - c^{n+\frac{1}{2}}), \tag{85}$$

we derive the discrete mass conservation law (78) from Eq. (82). □

Theorem 3.5. *The nonlinear scheme* (71)-(74) *satisfies the following discrete energy conservation law:*

$$\begin{aligned} E_{\bar{t}} = &- \tilde{\sigma} M(c^{n+\frac{1}{2}})\|\nabla \mu^{n+\frac{1}{2}} + \alpha \nabla p^{n+\frac{1}{2}}\|^2 \\ &- \nu(c^{n+\frac{1}{2}})\|\nabla \bar{\boldsymbol{u}}^{n+\frac{1}{2}}\|^2 - \frac{1}{3}\nu(c^{n+\frac{1}{2}})\|\nabla \cdot \bar{\boldsymbol{u}}^{n+\frac{1}{2}}\|^2 \le 0, \end{aligned} \tag{86}$$

where

$$E^n = \int\limits_{\Omega} \left(\frac{1}{2}\rho^n|\boldsymbol{u}^n|^2 + \rho^n gz + \frac{\tilde{\sigma}\epsilon}{2}|\nabla c^n|^2 + \tilde{\sigma} F(c^n)\right)d\boldsymbol{x} \tag{87}$$

is the total energy of the discrete system.

Proof. Taking the inner produce of Eqs. (71) with $\bar{\boldsymbol{u}}^{n+\frac{1}{2}}$, and adding them together we obtain

$$\begin{aligned} \frac{1}{2}\left(\rho|\boldsymbol{u}|^2\right)_{\bar{t}} = &- \nu(c^{n+\frac{1}{2}})|\nabla \bar{\boldsymbol{u}}^{n+\frac{1}{2}}|^2 - \frac{1}{3}\nu(c^{n+\frac{1}{2}})|\nabla \cdot \bar{\boldsymbol{u}}^{n+\frac{1}{2}}|^2 \\ &- \bar{\boldsymbol{u}}^{n+\frac{1}{2}} \cdot \nabla p^{n+\frac{1}{2}} - \tilde{\sigma} c^{n+\frac{1}{2}} \nabla \mu^{n+\frac{1}{2}} \cdot \bar{\boldsymbol{u}}^{n+\frac{1}{2}} \\ &- \rho^{n+\frac{1}{2}} g\boldsymbol{z} \cdot \bar{\boldsymbol{u}}^{n+\frac{1}{2}}, \end{aligned} \tag{88}$$

where we have applied the following identity with B.C. (36):

$$\begin{aligned} &\int\limits_{\Omega} \left(\rho^{n+\frac{1}{2}} \boldsymbol{u}^{n+\frac{1}{2}} \cdot \nabla \bar{\boldsymbol{u}}^{n+\frac{1}{2}} \cdot \bar{\boldsymbol{u}}^{n+\frac{1}{2}} + \frac{1}{2}\nabla \cdot (\rho^{n+\frac{1}{2}}\boldsymbol{u}^{n+\frac{1}{2}})\bar{\boldsymbol{u}}^{n+\frac{1}{2}} \cdot \bar{\boldsymbol{u}}^{n+\frac{1}{2}}\right)\mathrm{d}\boldsymbol{x} \\ &= \int\limits_{\Omega} \frac{1}{2}\nabla \cdot \left(\rho^{n+\frac{1}{2}} \boldsymbol{u}^{n+\frac{1}{2}} |\bar{\boldsymbol{u}}^{n+\frac{1}{2}}|^2\right)\mathrm{d}\boldsymbol{x} = 0. \end{aligned} \tag{89}$$

Applying the following identity and the discrete mass conservation (78),

$$\begin{aligned} &\int\limits_{\Omega} \rho^{n+\frac{1}{2}} g\boldsymbol{z} \cdot \bar{\boldsymbol{u}}^{n+\frac{1}{2}}\, d\boldsymbol{x} = \int\limits_{\Omega} \rho^{n+\frac{1}{2}} g\bar{\boldsymbol{u}}^{n+\frac{1}{2}} \cdot \nabla z\, d\boldsymbol{x} \\ &= -\int\limits_{\Omega} gz\nabla \cdot \left(\rho^{n+\frac{1}{2}}\bar{\boldsymbol{u}}^{n+\frac{1}{2}}\right)\, d\boldsymbol{x} = \int\limits_{\Omega} \rho_{\bar{t}} gz\, d\boldsymbol{x}, \end{aligned} \tag{90}$$

we rewrite Eq. (88) as

$$\begin{aligned} \left(\frac{1}{2}\rho|\boldsymbol{u}|^2 + \rho gz\right)_{\bar{t}} = &- \bar{\boldsymbol{u}}^{n+\frac{1}{2}} \cdot \nabla p^{n+\frac{1}{2}} - \tilde{\sigma} c^{n+\frac{1}{2}} \nabla \mu^{n+\frac{1}{2}} \cdot \bar{\boldsymbol{u}}^{n+\frac{1}{2}} \\ &- \nu(c^{n+\frac{1}{2}})|\bar{\boldsymbol{u}}^{n+\frac{1}{2}}|^2 - \frac{1}{3}\nu(c^{n+\frac{1}{2}})|\nabla \cdot \bar{\boldsymbol{u}}^{n+\frac{1}{2}}|^2. \end{aligned} \tag{91}$$

Taking the inner product of Eq. (72) with $p^{n+\frac{1}{2}}$, we obtain

$$\begin{aligned} \left(\nabla \cdot \bar{\boldsymbol{u}}^{n+\frac{1}{2}}\right) p^{n+\frac{1}{2}} = &- \alpha\tilde{\sigma} M(c^{n+\frac{1}{2}}) \left(\nabla \mu^{n+\frac{1}{2}} \cdot \nabla p^{n+\frac{1}{2}}\right) \\ &- \alpha^2\tilde{\sigma} M(c^{n+\frac{1}{2}})|\nabla p^{n+\frac{1}{2}}|^2. \end{aligned} \tag{92}$$

Taking the inner product of Eq. (73) with $\mu^{n+\frac{1}{2}}$, we obtain

$$\begin{aligned} c_{\bar{t}}\mu^{n+\frac{1}{2}} - c^{n+\frac{1}{2}}\nabla \mu^{n+\frac{1}{2}} \cdot \bar{\boldsymbol{u}}^{n+\frac{1}{2}} = &- \tilde{\sigma} M(c^{n+\frac{1}{2}})|\nabla \mu^{n+\frac{1}{2}}|^2 \\ &- \alpha\tilde{\sigma} M(c^{n+\frac{1}{2}})\nabla p^{n+\frac{1}{2}} \cdot \nabla \mu^{n+\frac{1}{2}}. \end{aligned} \tag{93}$$

Taking the inner product of Eq. (74) with $c_{\bar{t}}$, we obtain

$$\mu^{n+\frac{1}{2}} c_{\bar{t}} = \left(\tilde{\sigma} F(c) + \frac{\epsilon \tilde{\sigma}}{2} |\nabla c|^2 \right)_{\bar{t}}. \tag{94}$$

Combine Eqs. (91)-(94), we obtain the energy stability of our numerical method, Eq. (86). □

Remark 3.2. For constant density model, the unique solvability could be established with the help of Browder-Minty lemma and the monotonicity analysis, by using semi-implicit approximation to the fluid convective term. Meanwhile, for the variable density system, an evolutionary equation for the variable of u^2 is needed to construct structure-preserving schemes, and such an effort leads to a numerical system involved with a fully implicit treatment for the fluid convective term. As a result, the unique solvability analysis could hardly be theoretically justified. On the other hand, extensive numerical experiments have indicated no trouble for the numerical solution, provided that the time step size is sufficiently small.

Remark 3.3. Although we consider only time-discretization schemes, since the stability proofs are all based on variational formulations with the same space for trial and test functions, we can combine these semi-discrete schemes with any consistent Galerkin type approximations or some special finite difference discretization [20] in space to construct fully discrete energy stable schemes.

Remark 3.4. Due to the limitation of unique solvability for highly nonlinear scheme (32)-(35) which also results in big difficulty in making convergence analysis. We will discuss this issue in the future work. Some related works about Cahn-Hilliard-Navier-Stokes or Cahn-Hilliard-Helw-Shaw systems are established in [21–23].

4. Implementations

All the numerical schemes are discretized spatially by using a finite difference scheme on staggered grid, and is computed by using a block structured adaptive FAS multigrid (BSAM2.0 [18]) numerical package. Here we briefly show some basic definitions and notations for the finite difference discretization on a staggered grid. We refer [12] for details of the implementations. In two dimensional, let $\Omega = (0, L_x) \times (0, L_y)$, with $L_x = m_1 \times h$ and $L_y = m_2 \times h$, where m_1 and m_2 are positive integers and $h > 0$ is the spatial step size. For simplicity we assume that $L_x = L_y$. Consider the following four sets

$$E_{m_1} = \{x_{i+\frac{1}{2}} | i = 0, ..., m_1\}, \tag{95}$$

$$E_{\bar{m}_1} = \{x_{i+\frac{1}{2}} | i = -1, ..., m_1 + 1\}, \tag{96}$$

$$C_{m_1} = \{x_i | i = 1, ..., m_1\}, \tag{97}$$

$$C_{\bar{m}_1} = \{x_i | i = 0, ..., m_1 + 1\}, \tag{98}$$

where $x_{i+\frac{1}{2}} = i \times h$ and $x_i = (i - \frac{1}{2}) \times h$. Here E_{m_1} and $E_{\bar{m}_1}$ are called uniform partition of $[0, L_x]$ of size m_1, and its elements are called edge-centered points. The two points belonging to $E_{\bar{m}_1}/E_{m_1}$ are called ghost points. The elements of $C_{\bar{m}_1}$ and C_{m_1} are called cell-centered points. Again, the two points belonging to $C_{\bar{m}_1}/C_{m_1}$ are called ghost points. Analogously, the sets E_{m_i} and $E_{\bar{m}_2}$ contain the edge-centered points, and C_{m_2} and $C_{\bar{m}_2}$ contain the cell-centered points of the interval $[0, L_y]$. We then define the following functions spaces:

$$C_{m_1 \times m_2} = \{\phi : C_{m_1} \times C_{m_2} \to \boldsymbol{R}\}, \tag{99}$$

$$E^{ew}_{m_1 \times m_2} = \{u : E_{m_1} \times C_{m_2} \to \boldsymbol{R}\}, \tag{100}$$

$$E^{ns}_{m_1 \times m_2} = \{v : C_{m_1} \times E_{m_2} \to \boldsymbol{R}\}, \tag{101}$$

for cell-centered functions, east–west edge-centered functions and north–south edge-centered functions respectively. In this paper, the cell-centered functions are the phase variable ϕ, chemical potential μ, and pressure p, the east–west edge-centered function is the x-component of the velocity, u, and the north–south edge-centered function is the y-component of the velocity, v.

Here, we briefly show the implementations of Scheme 1. As Scheme 1, Eqs. (32)-(35), is a highly nonlinear system, we employ Newton's method to linearize the whole system. To solve the Navier-Stokes equations (32) and (33), we use the Vanker smoother by treating them as a system of five unknowns on a staggered grid, namely $(u_{i-\frac{1}{2},j}, u_{i+\frac{1}{2},j}, v_{i,j-\frac{1}{2}}, v_{i,j+\frac{1}{2}}, p_{i,j})$ on each staggered grid. Together with Eqs. (34) and (35), we obtain $(u_{i-\frac{1}{2},j}, u_{i+\frac{1}{2},j}, v_{i,j-\frac{1}{2}}, v_{i,j+\frac{1}{2}}, p_{i,j}, c_{i,j}, \mu_{i,j})$ simultaneously for each staggered grid. Note that this implementation can be extended to three dimensional straightforwardly.

Table 1
The L^2 errors of the velocities u, v and phase field variable c in a rising drop example in Sec. 5.1, see text for details.

δt	$error_u$	k	$error_v$	k	$error_c$	k
5.0×10^{-3}	6.53×10^{-5}	–	6.34×10^{-5}	–	7.32×10^{-4}	–
2.5×10^{-3}	1.98×10^{-5}	1.72	2.03×10^{-5}	1.64	2.13×10^{-4}	1.78
1.25×10^{-4}	5.30×10^{-6}	1.90	5.60×10^{-6}	1.86	5.59×10^{-5}	1.93
6.25×10^{-4}	1.35×10^{-6}	1.98	1.42×10^{-6}	1.99	1.39×10^{-5}	2.01

5. Numerical results

Although three numerical schemes are developed here, we use Scheme 1 for most of the simulations. As Schemes 1 and 2 are very similar, we then compare the Schemes 2 and 3 through section 5.2.

5.1. Convergence test

In this subsection, we test the convergence rate of Scheme 1 (32)-(35) through a rising drop example, where we assume that there is a light fluid drop placed inside a heavy fluid. With the effect of gravity, the drop will rise. The computational domain is set to be $\Omega = [0,1]^2$, where the light drop of radius 0.2 is centered initially at $(x = 0.5,\ \ y = 0.3)$. We impose the no-slip boundary conditions for velocity $\boldsymbol{u}$, and no-flux boundary conditions for c and μ. Moreover, we set all the parameters to be

$$\mu_1 = 1,\ \ \mu_2 = 3,\ \ \rho_1 = 1,\ \ \rho_2 = 3,\ \ \sigma = 0.1,\ \ g = 1 \text{ and } \epsilon = 0.01. \tag{102}$$

Note that, we use the following units: μ (kg/m s), ρ (kg/m^3), g (m/s^2), σ (kg/s^2). for all the computations in §5.

The initial condition for the phase variable is given as

$$c(x, y, 0) = \frac{1}{2}\left(1 - \tanh\left(\frac{\sqrt{(x-0.5)^2 + (y-0.3)^2} - 0.2}{2\sqrt{2}\epsilon}\right)\right). \tag{103}$$

In the convergence test, we fix the mesh size as 1024 × 1024 and set the initial time step as $\delta t = 0.01$. We then refine the time step by 2 and collect the solutions of phase variable ϕ and velocity $\boldsymbol{u}$ at $t = 1$. We finally calculate the L^2-norm errors and the convergence rate, where the errors are calculated as the difference between the solution of coarse time step and that of the adjacent finner time step. It is observed from Table 1 that our numerical method is second-order convergence in time for both variables.

To further validate our numerical solver, we consider a numerical test that was originally computed in [24]. In particular, we assume that there is a square domain $\Omega = [0,1]^2$, in which a circle of radius $r = 0.15$, initially centered at $(0.5, 0.75)$ is deformed under a solenoidal velocity field:

$$u(x, y, t) = -\sin^2(\pi x)\sin(2\pi y)\cos(\pi t/T), \tag{104}$$

$$v(x, y, t) = \sin^2(\pi y)\sin(2\pi x)\cos(\pi t/T). \tag{105}$$

By doing this, the flow field reverses in time such that any fluid body returns to its initial position at time T, allowing the error to be quantified as:

$$Err = \int_{\Omega} |c_{n1} - c_{n2}| \mathrm{d}\boldsymbol{x}. \tag{106}$$

Convergence studies are performed for three different values of T on fixed uniform grids. Again Scheme 1 is considered in this section. Fig. 1 shows the reconstructed interfaces for the three values of T. Quantitative error measurements and convergence rates are shown in Table 2. Here we fixed the value of $\epsilon = 0.01$, and refine the mesh size n and time step Δt together. The convergence rates show that our numerical method is second order accurate, even when T is large, for which large complex topological change has occurred (see Fig. 2), indicating that our method is remarkably resilient for interface capturing.

In Fig. 3, we show the evolution of the circular fluid body in the single vortex flow field Eqs. (104) and (105) without multiplying the cosing functions. It is seen that the fluid body is spun into a thinning filament, which compares very well with those results obtained using other methods, for example [25,24,26,27]. Theoretically, the filament spirals toward the vortex center, and becomes thinner and thinner continuously. Here we set $\epsilon = 0.005$, which stands for a thinner interface. Fig. 2 shows that the thin filament breaks into small pieces beginning at its tail after long time evolution. This is because the grid resolution has become low relative to the thinning filament when the thickness of the filament is equal to or less than the grid size. Because the interface is represented by a single line segment in each interfacial grid cell, any

Table 2
L_1 error norms, convergence rates and time averaged mass errors for the time-reversed, single vortex test. See text for details.

T	n	L_1 error	order	Mass error
0.5	256	1.757×10^{-3}		$< 10^{-14}$
0.5	512	4.567×10^{-4}	1.86	$< 10^{-14}$
0.5	1024	1.142×10^{-4}	2.00	$< 10^{-14}$
2.0	256	5.053×10^{-3}		$< 10^{-14}$
2.0	512	1.400×10^{-3}	1.85	$< 10^{-14}$
2.0	1024	3.465×10^{-4}	2.00	$< 10^{-14}$
8.0	256	1.732×10^{-2}		$< 10^{-14}$
8.0	512	4.651×10^{-3}	1.90	$< 10^{-14}$
8.0	1024	1.131×10^{-3}	2.01	$< 10^{-14}$

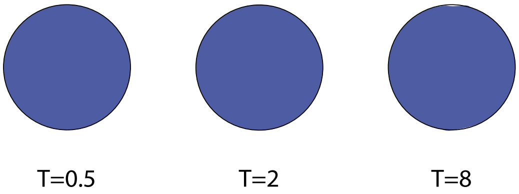

Fig. 1. The reconstructed interfaces of an initially circular fluid body in a single vortex flow at t=T.

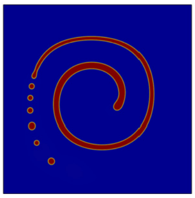

Fig. 2. The interface at $t = 4$ of an initially circular fluid body in a single vortex flow with velocity field defined in Eqs. (104) and (105) with T=8.

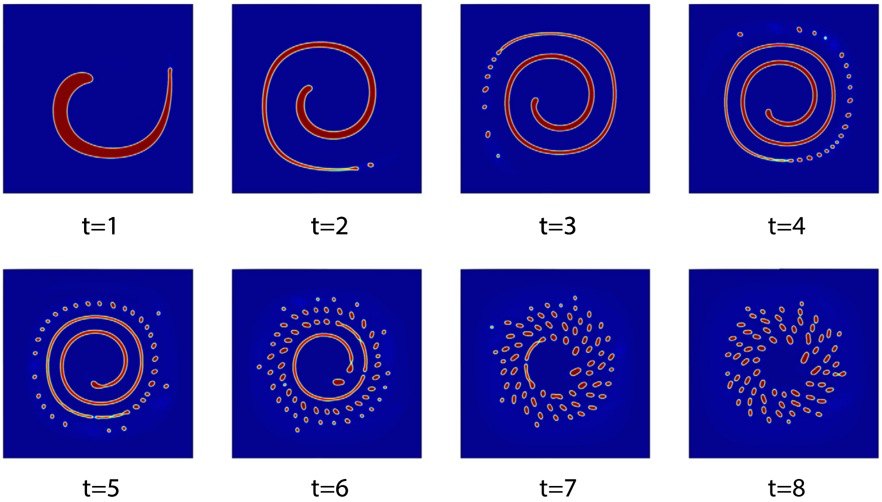

Fig. 3. Evolution of an initially circular fluid body in a single vortex flow with velocity field defined in Eqs. (104) and (105) without multiplying the cosing functions.

two interfaces merge automatically whenever they come into the same cell, resulting in an nonphysical ‘pinch-off’. Once the pinch-off occurs, the linear segment approximation of an interface immediately flattens the high curvature region, effectively applying numerical surface tension.

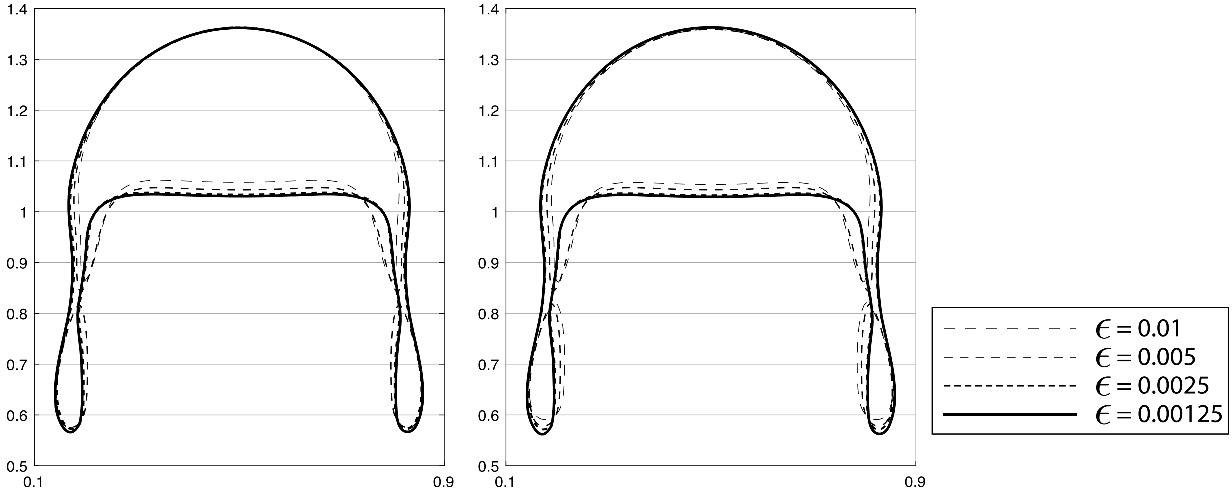

Fig. 4. Bubble shapes at time $t = 3$ for different ϵ. Left: Scheme 2, Right: Scheme 3.

5.2. Rising bubble

Here we test our numerical Schemes 2 and 3 by calculating an example with an air bubble rising in the water [28,29]. The computational domain is $[0, 1] \times [0, 2]$. Four grid sizes, namely 64×128, 128×256, 256×512 and 512×1024 are used for different values of ϵ =(0.01, 0.005, 0.0025, 0.00125) respectively. On all the domain boundaries, no-slip boundary conditions are imposed for $\boldsymbol{u}$, and no-flux boundary conditions are imposed for c and μ. The air bubble is of radius $r = 0.25$ with center located at $(0.5, 0.5)$ initially. The corresponding initial condition for phase variable is given as

$$c = \frac{1}{2}\left(1 + \tanh\left(\frac{\sqrt{(x-0.5)^2 + (y-0.5)^2} - r}{2\sqrt{2}\epsilon}\right)\right). \tag{107}$$

We set all the parameters to be

$$\rho_1 = 1, \quad \rho_2 = 1000, \quad \mu_1 = 0.1, \quad \mu_2 = 10, \quad g = 0.98, \quad \sigma = 1.96. \tag{108}$$

Fig. 4 shows the bubble shapes at time $(t = 3)$ with different values of ϵ obtained by using Schemes 2 and 3. The bubble shapes differ clearly for different values of ϵ but seem to converge. The break off can be observed for certain values of $\epsilon (= 0.005, 0.01)$. However, it remains unclear if break off really should occur for this setting [28,29]. In particular, another diffuse interface model is calculated in [29], where no break-off is observed when the ϵ is small enough. It is clearly not sufficient to only look at the bubble shapes, therefore we use the previously defined benchmark quantities, namely the center mass and rising velocity, and plot them over time in Figs. 5 and 6. All the quantities seem to converge. Furthermore, we show the free energy dissipation in Fig. 7, where, again, for all the values of ϵ the energy dissipates and the curves seem to converge. As we mentioned in Remark 2.1, the quasi-incompressibility is derived from the mass conservation and it is thus to ensure the mass conservation of the mixture and the single component. We then checked the mass evolution of the single components $\int_\Omega \rho_1 \phi^n \, \mathrm{d}\boldsymbol{x}$ and the mixture $\int_\Omega \rho^n \, \mathrm{d}\boldsymbol{x}$, and it has been confirmed that all the masses have been conserved upto 10^{-14} during the computations.

5.3. Three dimensional two-bubble merger problem

In our last example, the merger of two spherical bubbles is simulated coaxially and obliquely in the domain of $[0, 0.04] \times [0, 0.04] \times [0, 0.08]$ m^3 with a uniform grid $128 \times 128 \times 256$. We set time step as $\delta t = 10^{-3}$. The initial bubbles have a radius of 0.005 m. On all the domain boundaries, no-slip boundary conditions are imposed for $\boldsymbol{u}$, and no-flux boundary conditions are imposed for c and μ. The upper bubble is centered at positions $[0.02, 0.02, 0.025]$, and the lower bubble is centered at $[0.02, 0.02, 0.015]$ and $[0.028, 0.02, 0.015]$ respectively for the coaxial and the oblique coalescence experiments. We set all the parameters as follows:

$$\begin{aligned} &\epsilon = 0.005, \; g = 9.8, \; \rho = 1, \; \rho_2 = 1000, \; \mu_1 = 3.23 \times 10^{-3}, \; \mu_2 = 3.23 \times 10^{-1}, \\ &R = 0.005, \; \sigma = 0.0153. \end{aligned} \tag{109}$$

Such that the non-dimensional parameters with the Morton number of $Mo = g\mu_2^4 \Delta\rho / \rho_2^2 \sigma^3 = 30$, and the Eövtös number of Eö$= g\Delta\rho R^2/\sigma = 16$. Scheme 1 is employed for the simulation in this section. The numerical results are shown in Fig. 8,

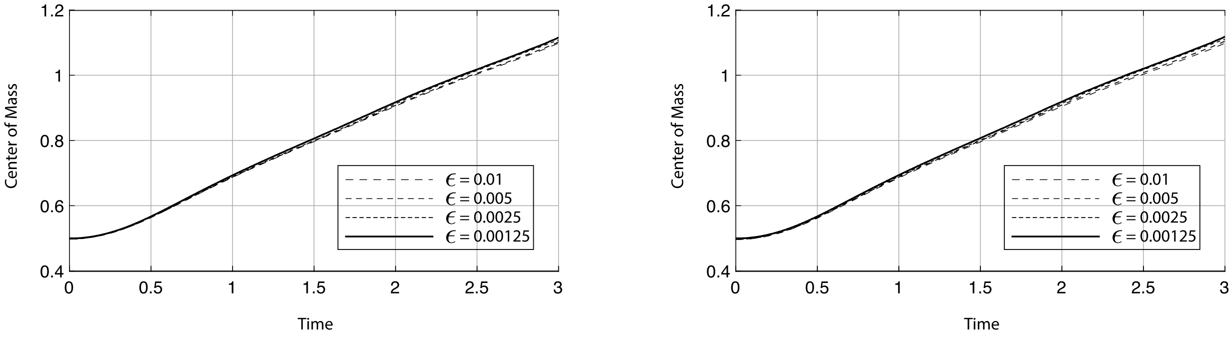

Fig. 5. Center of mass over time. Left: Scheme 2, Right: Scheme 3.

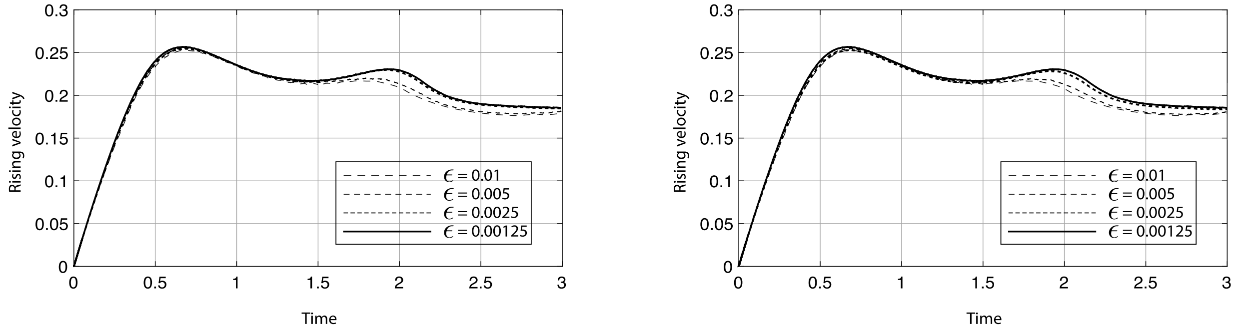

Fig. 6. Rising velocity over time. Left: Scheme 2, Right: Scheme 3.

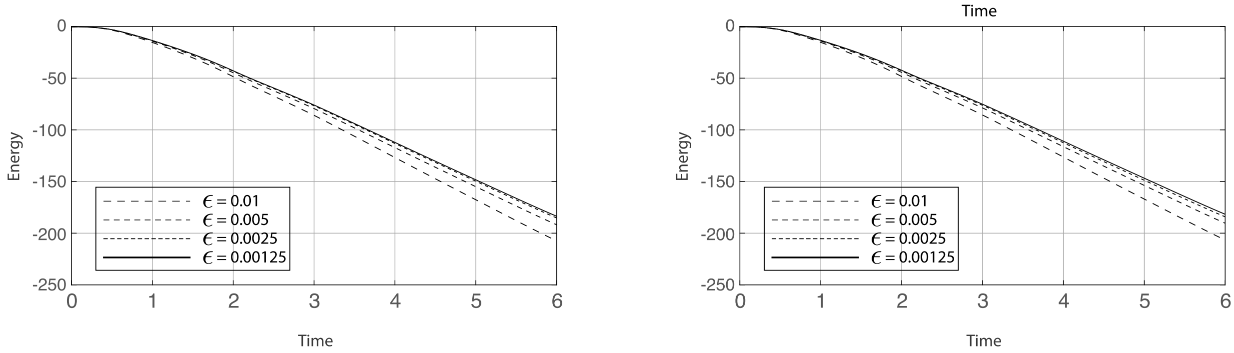

Fig. 7. Free energy over time. Left: Scheme 2, Right: Scheme 3.

where we can observe good agreement with the experimental observation in [30] and the numerical results in [31]. The deformation and acceleration of the lower bubble in z-direction can be seen when the lower bubble enters into the wake region of upper bubble. The reason for this observation is that the drag force on lower bubble becomes smaller than the upper bubble before the coalescence the two bubbles.

5.4. Rayleigh-Taylor instability in 3D

Our next test is the Rayleigh-Taylor instability (RTI) which would occur for any perturbation along the interface between a heavy fluid ($c = 0$ for fluid 2) on top of a light fluid ($c = 1$ for fluid 1). The instability is characterized by the non-dimensional parameter Atwood ratio, that $At = (\rho_2 - \rho_1)/(\rho_2 + \rho_1)$. Here we test our code in 3 dimensional with the initial interface being located in a cuboid domain $[0, L] \times [0, L] \times [0, 4L]$ at $\tilde{z}(x, y, z) = 2L + 0.05L\,(\cos(2\pi x/L) + \cos(2\pi y/L))$, which represents a planar interface superimposed by a perturbation with amplitude $0.1L$. Here we set $L = 1$ and

$$c = \frac{1}{2}\left(1 - \tanh\left(\frac{z - \tilde{z}}{2\sqrt{2}\epsilon}\right)\right). \tag{110}$$

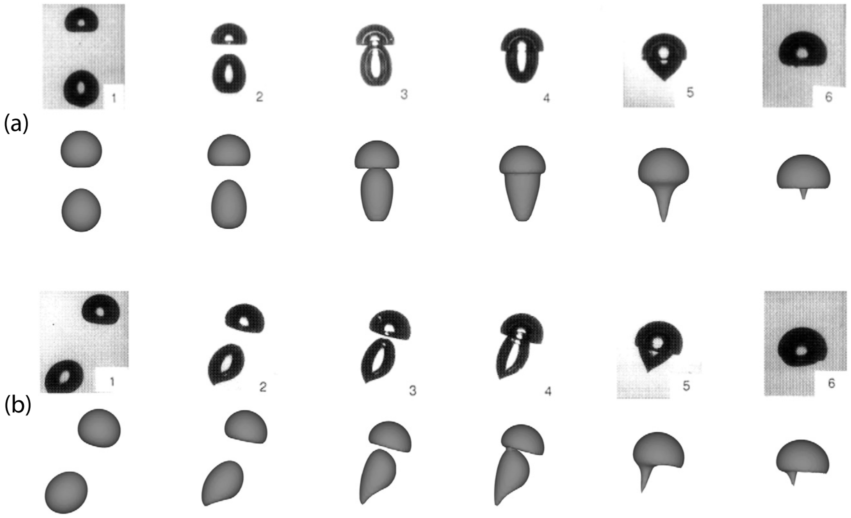

Fig. 8. Comparison between the experimental observations from [30] and numerical predictions for coaxial and oblique coalescence of two bubbles: $Mo = 30$, $E\ddot{o} = 16$. The experimental results are taken at every 0.03 second.

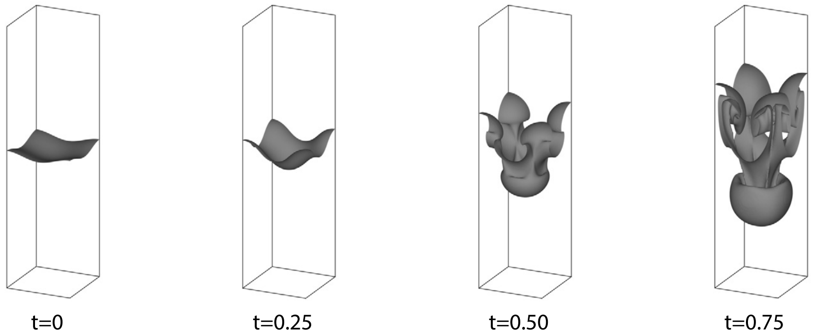

Fig. 9. Evolution of the interface with the Atwood number of 0.5. The interface is viewed from the heavy fluid side.

We set all the parameters as

$$\rho_1 = 1, \quad \rho_2 = 3, \quad At = 0.5, \quad \nu_1 = \nu_2 = 0.001, \quad g = 9.8, \quad \sigma = 0, \quad \epsilon = 0.005. \tag{111}$$

Periodic boundary conditions are imposed on the left, right, front and back boundaries for $\boldsymbol{u}$, c and μ. At the top and bottom boundaries, we impose the no-slip boundary condition for $\boldsymbol{u}$, and no-flux boundary conditions for c and μ. A uniform grid $[128 \times 128 \times 512]$ is used, and we set time step to be $\delta t = 10^{-3}$. Scheme 1 is employed for the simulation in this section.

The evolution of the interface are shown in Fig. 9. During the early stages, the interface grows nearly symmetrically up and down and remains rather simple. But, as time goes by, it becomes more complicated and spikes of the heavy fluid first form near the middle of the four sides of the computational domain. The roll-up at the edge of the spike starts at a later time. At $t = 0.75$, these roll-ups are stretched into two extra layers of the heavy fluid folded upward. This two-layer roll-up phenomenon is a unique feature of the three-dimensional RTI, where the similar results are obtained in [32].

6. Conclusion

We develop in this paper three new second order accurate numerical methods to solve two-phase flow using the quasi-incompressible NSCH system with a variable density. Through several numerical examples, we also demonstrate that our numerical methods can capture the interface breakup and collisions smoothly even with a large density and viscosity ratio. Simulations also confirm that the discrete energy functional is non-increasing, as predicted by our theory. Moreover, the pinch-off event is smoothly captured by numerical schemes. In the case of the rising bubble, we show that numerical results which are consistent with the experimental results.

Scheme 1 only enjoys the property of mass conservation. While Scheme 2 and Scheme 3 have properties of mass conservative and energy decreasing in discrete level. We have performed numerical simulations using three schemes proposed above and validate the effectiveness and accuracy in numerical part. For a mild density ratio, Scheme 1 is recommended to use due to its simplicity which is constructed based on the original form of quasi-incompressible NSCH system. While, we recommend Scheme 2 and Scheme 3 to solve the quasi-incompressible NSCH system with larger density ratio in which an extremely small time step must be used for Scheme 1. In future work, we will perform extensive studies of the two-phase problems with more complicated interface dynamics, e.g., moving contact line problems, where the fluid/fluid interface interacts with solid wall, and the dynamics of interface with Marangoni effects, where surface tension gradients are induced by in-homogeneous temperature distributions or surfactants that can be absorbed at the liquid/gas or liquid/liquid interfaces.

CRediT authorship contribution statement

Zhenlin Guo and Qing Cheng: Conceptualization, Methodology, Writing – Original draft preparation. Ping Lin, Chun Liu and John Lowengrub: Contribution of ideas, Revising and Editing.

Declaration of competing interest

The authors declare that they have no known competing financial interests or personal relationships that could have appeared to influence the work reported in this paper.

References

[1] Z. Guo, F. Yu, P. Lin, S. Wise, J. Lowengrub, A diffuse domain method for two-phase flows with large density ratio in complex geometries, J. Fluid Mech. (2020).

[2] H. Abels, H. Garcke, G. Grün, Thermodynamically consistent, frame indifferent diffuse interface models for incompressible two-phase flows with different densities, Math. Models Methods Appl. Sci. 22 (03) (2012) 1150013, https://doi.org/10.1142/s0218202511500138.

[3] F. Boyer, A theoretical and numerical model for the study of incompressible mixture flows, Comput. Fluids 31 (1) (2002) 41–68, https://doi.org/10.1016/S0045-7930(00)00031-1, http://www.sciencedirect.com/science/article/pii/S0045793000000311.

[4] H. Ding, P.D. Spelt, C. Shu, Diffuse interface model for incompressible two-phase flows with large density ratios, J. Comput. Phys. 226 (2) (2007) 2078–2095, https://doi.org/10.1016/j.jcp.2007.06.028, http://www.sciencedirect.com/science/article/pii/S0021999107002793.

[5] J. Lowengrub, L. Truskinovsky, Quasi-incompressible Cahn–Hilliard fluids and topological transitions, Proc. R. Soc. Lond. A (1998), http://citeseerx.ist.psu.edu/viewdoc/summary?doi=10.1.1.232.8527.

[6] J. Shen, X. Yang, A phase-field model and its numerical approximation for two-phase incompressible flows with different densities and viscosities, SIAM J. Sci. Comput. 32 (3) (2010) 1159–1179, https://doi.org/10.1137/09075860x.

[7] J. Shen, X. Yang, Q. Wang, Mass and volume conservation in phase field models for binary fluids, Commun. Comput. Phys. 13 (4) (2013) 1045–1065, https://doi.org/10.4208/cicp.300711.160212a.

[8] M. Shokrpour Roudbari, G. Şimşek, E.H. van Brummelen, K.G. van der Zee, Diffuse-interface two-phase flow models with different densities: a new quasi-incompressible form and a linear energy-stable method, Math. Models Methods Appl. Sci. 28 (04) (2018) 733–770, https://doi.org/10.1142/s0218202518500197.

[9] G.L. Aki, W. Dreyer, J. Giesselmann, C. Kraus, A quasi-incompressible diffuse interface model with phase transition, 2014.

[10] J. Li, Q. Wang, A class of conservative phase field models for multiphase fluid flows, J. Appl. Mech. 81 (2) (Sep 2013), https://doi.org/10.1115/1.4024404.

[11] Q. Cheng, X. Yang, J. Shen, Efficient and accurate numerical schemes for a hydro-dynamically coupled phase field diblock copolymer model, J. Comput. Phys. 341 (2017) 44–60.

[12] Z. Guo, P. Lin, J. Lowengrub, S. Wise, Mass conservative and energy stable finite difference methods for the quasi-incompressible Navier–Stokes–Cahn–Hilliard system: primitive variable and projection-type schemes, Comput. Methods Appl. Mech. Eng. 326 (2017) 144–174, https://doi.org/10.1016/j.cma.2017.08.011, http://www.sciencedirect.com/science/article/pii/S0045782517303729.

[13] H. Garcke, M. Hinze, C. Kahle, A stable and linear time discretization for a thermodynamically consistent model for two-phase incompressible flow, Appl. Numer. Math. 99 (2016) 151–171, https://doi.org/10.1016/j.apnum.2015.09.002, http://www.sciencedirect.com/science/article/pii/S0168927415001324.

[14] G. Grün, F. Klingbeil, Two-phase flow with mass density contrast: stable schemes for a thermodynamic consistent and frame-indifferent diffuse-interface model, J. Comput. Phys. 257 (2014) 708–725, https://doi.org/10.1016/j.jcp.2013.10.028, http://www.sciencedirect.com/science/article/pii/S0021999113007043.

[15] Y. J, K. J, A phase-field method for two-phase fluid flow in arbitrary domains, Comput. Math. Appl. 79 (6) (2020) 1857–1874.

[16] M. Shokrpour Roudbari, G. Şimşek, E.H. van Brummelen, K.G. van der Zee, Diffuse-interface two-phase flow models with different densities: a new quasi-incompressible form and a linear energy-stable method, Math. Models Methods Appl. Sci. 28 (04) (2018) 733–770.

[17] Q. Cheng, C. Liu, J. Shen, A new Lagrange multiplier approach for gradient flows, Comput. Methods Appl. Mech. Eng. 367 (2020) 113070.

[18] W. Feng, Z. Guo, J.S. Lowengrub, S.M. Wise, A mass-conservative adaptive fas multigrid solver for cell-centered finite difference methods on block-structured, locally-Cartesian grids, J. Comput. Phys. 352 (2018) 463–497.

[19] Q. Cheng, C. Liu, J. Shen, Generalized SAV approaches for gradient systems, J. Comput. Appl. Math. (2021) 113532.

[20] C. Wang, J.-G. Liu, Convergence of gauge method for incompressible flow, Math. Comput. 69 (232) (2000) 1385–1407.

[21] A.E. Diegel, C. Wang, X. Wang, S.M. Wise, Convergence analysis and error estimates for a second order accurate finite element method for the Cahn–Hilliard–Navier–Stokes system, Numer. Math. 137 (3) (2017) 495–534.

[22] W. Chen, Y. Liu, C. Wang, S. Wise, Convergence analysis of a fully discrete finite difference scheme for the Cahn-Hilliard-Hele-Shaw equation, Math. Comput. 85 (301) (2016) 2231–2257.

[23] Y. Liu, W. Chen, C. Wang, S.M. Wise, Error analysis of a mixed finite element method for a Cahn–Hilliard–Hele–Shaw system, Numer. Math. 135 (3) (2017) 679–709.

[24] N. Balcázar, L. Jofre, O. Lehmkuhl, J. Castro, J. Rigola, A finite-volume/level-set method for simulating two-phase flows on unstructured grids, Int. J. Multiph. Flow 64 (2014) 55–72, https://doi.org/10.1016/j.ijmultiphaseflow.2014.04.008, http://www.sciencedirect.com/science/article/pii/S030193221400072X.

[25] T.W. Sheu, C. Yu, P. Chiu, Development of a dispersively accurate conservative level set scheme for capturing interface in two-phase flows, J. Comput. Phys. 228 (3) (2009) 661–686, https://doi.org/10.1016/j.jcp.2008.09.032.

[26] Y. Sato, B. Niceno, A conservative local interface sharpening scheme for the constrained interpolation profile method, Int. J. Numer. Methods Fluids 70 (4) (2011) 441–467, https://doi.org/10.1002/fld.2695.

[27] X. Yang, A.J. James, J. Lowengrub, X. Zheng, V. Cristini, An adaptive coupled level-set/volume-of-fluid interface capturing method for unstructured triangular grids, J. Comput. Phys. 217 (2) (2006) 364–394, https://doi.org/10.1016/j.jcp.2006.01.007, http://www.sciencedirect.com/science/article/pii/S0021999106000143.

[28] S. Hysing, S. Turek, D. Kuzmin, N. Parolini, E. Burman, S. Ganesan, L. Tobiska, Quantitative benchmark computations of two-dimensional bubble dynamics, Int. J. Numer. Methods Fluids 60 (11) (2009) 1259–1288, https://doi.org/10.1002/fld.1934.

[29] S. Aland, A. Voigt, Benchmark computations of diffuse interface models for two-dimensional bubble dynamics, Int. J. Numer. Methods Fluids 69 (3) (2011) 747–761, https://doi.org/10.1002/fld.2611.

[30] G. Brereton, D. Korotney, Coaxial and oblique coalescence of two rising bubbles, in: Dynamics of Bubbles and Vortices Near a Free Surface, vol. 119, 1991, pp. 50–73.

[31] R. Denèfle, S. Mimouni, J. Caltagirone, S. Vincent, Multifield hybrid method applied to bubble rising and coalescence, Int. J. Comput. Methods Exp. Meas. 2 (1) (2014) 46–57.

[32] H.G. Lee, J. Kim, Numerical simulation of the three-dimensional Rayleigh–Taylor instability, Comput. Math. Appl. 66 (8) (2013) 1466–1474.